Ultrahigh piezoelectricity in lead-free piezoceramics by synergistic design

WANG, Dawei <http://orcid.org/0000-0001-6957-2494>, FAN, Zhongming, RAO, Guanghui, WANG, Ge, LIU, Yao, YUAN, Changlai, MA, Tao, LI, Dejun, TAN, Xiaoli <http://orcid.org/0000-0002-4182-663X>, LU, Zhilun, FETEIRA, Antonio <http://orcid.org/0000-0001-8151-7009>, LIU, Shiyu, ZHOU, Changrong and ZHANG, Shujun

Citation:

Copyright and re-use policy

Ultrahigh piezoelectricity in lead-free piezoceramics by synergistic design

Dawei Wang[a#]*, Zhongming Fan[b#], Guanghui Rao[c#], Ge Wang[a#], Yao Liu[d#], Changlai Yuan[c], Tao Ma[e], Dejun Li[f], Xiaoli Tan[b], Zhilun Lu[a], Antonio Feteira[g], Shiyu Liu[f]*, Changrong Zhou[c]*, Shujun Zhang[h]*

[a]Department of Materials Science and Engineering, University of Sheffield, Sheffield S1 3JD, UK

[b]Department of Materials Science and Engineering, Iowa State University, Ames, Iowa, 50011 USA

[c]Guangxi Key Laboratory of Information Materials, School of Material Science and Engineering, Guilin University of Electronic Technology, Guilin, Guangxi 541004, China

[d]Electronic Materials Research Lab, Key Lab of Education Ministry/International Center for Dielectric Research, School of Electronic and Information Engineering, Xi'an Jiaotong University, Xi'an 710049, China

[e]Ames Laboratory, U.S. Department of Energy, Ames, IA 50011, USA

[f]College of Physics and Materials Science, Tianjin Normal University, Tianjin 300387, China

[g]Christian Doppler Lab on Advanced Ferroic Oxides, Materials and Engineering Research Institute, Sheffield Hallam University, Sheffield S1 1WB, UK

[h]ISEM, Australian Institute for Innovative Materials, University of Wollongong, Wollongong, NSW 2500, Australia *Corresponding author. E-mail address: dawei.wang@sheffield.ac.uk, zcr750320@guet.edu.cn, buaasyliu@gmail.com, shujun@uow.edu.au

[#]Author contributions: These authors contributed equally to this work.

Abstract:

Following increased environmental concerns on the toxicity of lead, the discovery of ultrahigh piezoelectricity in lead-free piezoelectric materials is critical for the substitution of commercial lead zirconate titanate (PZT) ceramics in numerous electronics. In this work, a synergistic design strategy is proposed to enhance the piezoelectricity in lead-free piezoelectric materials by flattening the Gibbs free energy density profile, via the coexistence of multiple phases and local structural heterogeneity This strategic materials design approach is based on first-principles calculations combined with Landau phenomenological theory and phase field simulations. Sustainable Stannum-doped $BaTiO_3$ lead-free ferroelectric ceramics is prepared to validate our proposed mechanism, and a giant piezoelectric coefficient $d_{33} > 1100$ pC/N is achieved, being the highest value reported in lead-free piezoceramics. The mechanism and paradigm of the excellent piezoelectricity achieved here provides a feasible solution for replacing lead based piezoelectrics by lead-free counterparts.

**Keywords:** lead-free ceramics, piezoelectrics, dielectrics, $BaTiO_3$

Introduction

Piezoelectric materials convert mechanical stress to electric charge and vice-versa. This phenomenon originally demonstrated by the Curie brothers in 1880, has been vital for the successful operation of many advanced electronic devices such as micropositioning actuators, piezoelectric sensors, ultrasonic imaging transducers, to name a few.[1-3] For over sixty years, the piezoelectric materials market has been dominated by lead zirconate titanate $Pb(Zr,Ti)O_3$-based ceramics (PZTs), because they offer the best affordable combination of piezoelectric characteristics, i.e. the largest magnitude of piezoelectric coefficient (d), electromechanical coupling (k) and temperature stability. The excellent piezoelectric properties of ferroelectric PZT perovskite have been ascribed to the coexistence of rhombohedral (R) and tetragonal (T) phases at a morphotropic phase boundary (MPB).[1-3]

In the late 20th century, due to an ever increasing awareness of the hazardous effects of lead to human health and environment, its use became a subject of legal restrictions, such as the Restriction of Hazardous Substances Directive (RoHS) (2003) by the European Union, which particularly limits the usage of lead in electronic devices[4]. This prompted the search and development of lead-free piezoelectric ceramics which could be effective alternatives to PZT,[5-7] however, to date there is no lead-free piezoelectric able to totally replace PZT. There are a number of potential candidates such as $(K,Na)NbO_3$ (KNN), $Bi_{1/2}Na_{1/2}TiO_3$ (BNT), $(Ba,Ca)(Zr,Ti)O_3$ (BCZT) and $BiFeO_3$-$BaTiO_3$ (BF-BT), each of which exhibits strengths and weaknesses.[8-12] Extensive research on KNN based materials was originally triggered by Saito et al. in 2004, reporting textured $(K_{0.44}N_{a0.52}Li_{0.04})(Nb_{0.86}Ta_{0.10}Sb_{0.04})O_3$ ceramics with Curie temperature (T_C) of 253°C and high piezoelectric coefficient (d_{33}) = 416 pC/N.[13-19] Later, Liu and Ren reported an even higher d_{33} of 620 pC/N for $0.50Ba(Zr_{0.2}Ti_{0.8})O_3$-$0.50(Ba_{0.7}Ca_{0.3})TiO_3$ (BZT-50BCT),[20] which in that case was ascribed to the occurrence of a tri-critical point (TCP) consisting of T, R and cubic (C) phases. In 2015, Lee et al. reported a R-T MPB in quenched BF-BT with both high d_{33} (240-402 pC/N) and T_C (> 400 °C).[21]

A comparison of d_{33} *vs* T_C/T_m (where T_m is the temperature of maximum dielectric permittivity) for

3

lead-based and lead-free piezoelectric ceramics is plotted in Figure 1(a).[8-12] Generally, the values of d_{33} decrease with the increase of T_C/T_m, but clearly lead-based ceramics exhibit much larger d_{33} values than lead-free ceramics, which is still the main factor limiting the commercialization of lead-free ceramics. Recently, a new material design approach based on flattening the thermodynamic energy profile of ferroelectrics by local structural heterogeneity allowed to circumvent this so-called "ceiling effect" on high piezoelectricity in lead-free materials (Figure 1a). Indeed, this design approach was successfully applied to improve piezoactivity in Sm-doped $Pb(Mg_{1/3}Nb_{2/3})O_3$-$PbTiO_3$ (PMN-PT) ceramics (d_{33} > 1500 pC/N) and single-crystals (d_{33} ~ 4000 pC/N),[22,23]. Consequently, this has widened further the piezoelectric performance gap between lead and lead-free materials.
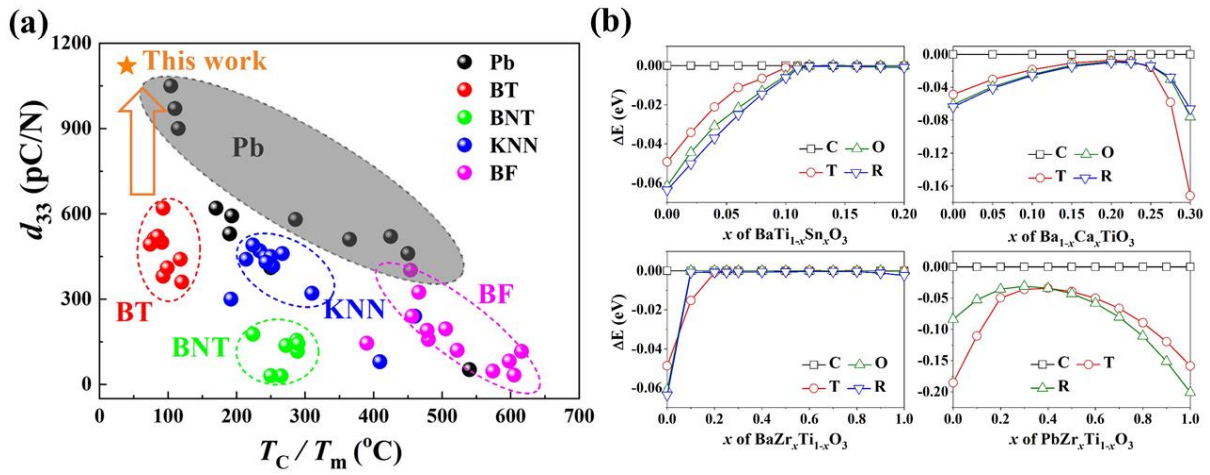
Figure 1 (a) A comparison of d_{33} *vs* T_C/T_m for piezoelectric ceramics. (b) The calculated the total-energy difference per unit cell ($\Delta E = E_i - E_C$, E_i: total energy of T, O and R phases; E_C: total energy of C phase) of C, T, O and R $BaTi_{1-x}Sn_xO_3$ (0≤x≤0.2), $Ba_{1-x}Ca_xTiO_3$ (0≤x≤0.3), $BaZr_xTi_{1-x}O_3$ (0≤x≤1) and $PbZr_xTi_{1-x}O_3$ (0≤x≤1).

Results and discussion

A synergistic strategy for high piezoelectricity: design, calculation and simulation

According to the Landau phenomenological theory,[22-26] a high d_{33} can be obtained via flattening of the Gibbs free-energy density profile with respect to polarization. This can be achieved either by a macroscopic coexistence of multiple phases (CMP) or by microscopic local structural heterogeneity (LSH). In principle, a combination of both mechanisms (CMP and LSH) can induce a greater enhancement of the intrinsic d_{33}, which to our knowledge has not yet been reported in lead-free materials.

A synergistic approach combining CMP and LSH was designed, and tried to break the high piezoelectricity "ceiling effect" in lead-free ceramics. In order to demonstrate the feasibility and significance of this approach, we selected Sn-doped BaTiO$_3$ (BT), as it contains no volatile or scarce elements. On cooling, the crystal structure of BT successively changes from C, T, O to R, as shown in Figure S1 (Supplemental Information). The C phase is a nonpolar phase, while T, O and R phases are polar phases with polarization vectors along [100], [101] and [111], respectively. Mathematically, the [100], [101] and [111] polarization vectors form a complete set of base vectors that spatially can express/represent any polarization vector under special stimuli conditions. Hence, CMP of T, O, R and C provides an ideal arrangement due to its mathematical completeness. This allows the construction of a four-phase CMP, which one could expect to provide the flattest thermodynamic energy profile and therefore enhanced piezoelectricity. From a mathematical viewpoint, complex multiple states with [100], [101], [111] polarization vectors and origin point at [000], corresponding to T, O, R and C phases, respectively, are preferred.

In this work, first-principles calculations combined with Landau free-energy theory are employed to realize the design of CMP in lead-free Sn-doped BT ceramics (BaTi$_{1-x}$Sn$_x$O$_3$, BTSx, $0 \leq x \leq 0.2$), which was strategically chosen to verify the feasibility of the aforementioned proof-of-concept. The total-energy (E) of T, O, R and C phase for BTSx was calculated separately by first-principles calculations, and the corresponding total-energy di□erence ($\Delta E = E_i - E_C$, i = T, O, R) between T, O, R and C phase as a function of Sn concentration is shown Figure 1(b). For pure BT, the order of structural stability is R > O > T > C, in agreement with the experimental observation of C-T-O-R phase transition upon cooling (Figure S1, Supplemental Information). With increasing Sn content, ΔE between R, T, O and C phases is found to decrease continuously, reaching zero at $x \geq 0.11$, suggesting the coexistence of R, T, O and C phases. This is further corroborated by the convergence of the calculated lattice parameters and volumes for different phase structures in BTSx (Figure S2a, Supplemental Information). In order to further appraise the proof-of-concept, ΔE values, lattice parameters and volumes of Ba$_{1-x}$Ca$_x$TiO$_3$ (BCxT), BaZr$_x$Ti$_{1-x}$O$_3$ (BZxT) and PbZr$_x$Ti$_{1-x}$O$_3$ (PZxT) were calculated from first-principles calculations and compared in Figure 1(b) and Figure S2

(Supplemental Information). Although BZxT and BTSx show similar CMP, i.e. R, O, T and C phases coexisting at x > 0.20, T_C of BZxT (x > 0.20) is below room temperature resulting in no piezoactivity at room temperature.[2,27] Furthermore, the total energy of C phase for BCxT and PZxT is always higher than that of R, O, T phases. Calculated lattice parameters and volumes never converge (Figure S2, Supplemental Information), ruling out coexistence of R, O, T and C phases in BCxT and PZxT, in contrast with BZxT and BTSx.

On the other hand, ferroelectrics may evolve into relaxor ferroelectrics (RFEs) by an increase of LSH, which is accompanied by the appearance of numerous polar nanoregions (PNRs) embedded in a non-polar matrix.[28] Due to the similar total energies between the non-polar phase (C) and the polar phases (R, O, T) in BTSx (x ≥ 0.11, Figure 1b), PNRs with multiple crystal symmetries (T, O, R) can be randomly nucleated, formed and embedded in the non-polar (C) matrix, which will have different polarization directions, as demonstrated by phase-field simulations shown in Figure 2(a,b). This arrangement of PNRs appears to be isotropic and macroscopically paraelectric (system with zero macroscopic polarization), which is consistent with the super-paraelectric model.[29] The Landau free-energy profile for polarization rotation of BTSx is shown in Figure 2(d). The spherical surface of the Landau free-energy in the polarization space suggests that the polar T, O and R phases may readily undergo rotation among the corresponding [100], [101] and [111] polarization directions (Figure 2(d,e)). The Landau free-energy profile of polarization extension for different polarization directions further indicates a low-barrier and nearly-free extension of the polarization direction (Figure 2f). Therefore, these multiphasic (T, O, R) PNRs in BTSx are easily re-orientable, re-extended and orderly re-arranged upon the application of a small external electric field (Figure 2b), which is expected to leadi to high piezoelectricity.
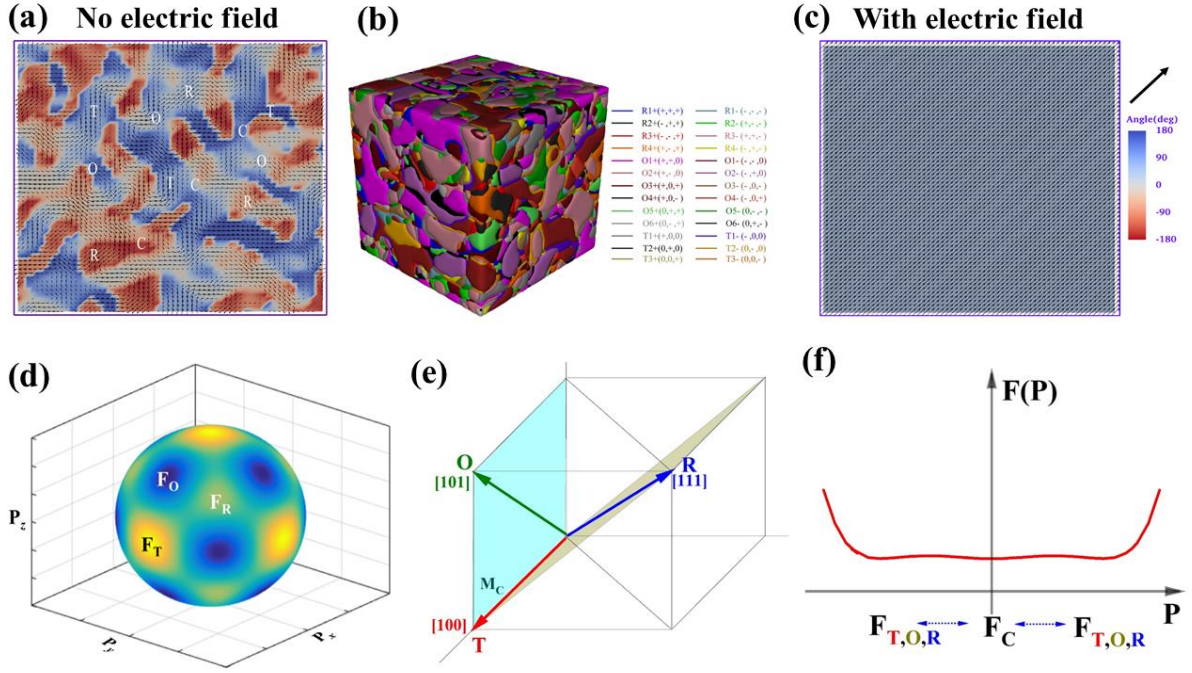
Figure 2 (a) Phase-field simulation of two-dimensional domain structure of RFEs with NPRs in nonpolar C phase without an external electric field. (b) Phase-field simulation of three-dimensional schematic of domain structure without an external electric field. (c) Phase-field simulation of two-dimensional domain structure of RFEs with an external electric field. (d) Three-dimensional schematic for the Landau free-energy profile of polarization rotation of RFEs for different polarizations within Landau theory under a four-phase coexistence condition. (e) Schematic of the respective [100], [101], and [111] polarization directions for the T, O, and R phases, respectively. (f) The Landau free-energy profiles of polarization extension for different polarization directions.

Structure and piezoelectricity of Sn-doped BT ceramics

Room temperature XRD patterns of BTSx in the 2θ range of 20°~70° are shown in Figure S3 (Supplemental Information) and several expanded diffraction peaks are given in Figure 3(a). Peaks are ascribed to either a single-phase perovskite or a mixture of perovskite phases, without any detectable secondary impurity phases. The shift of the diffraction peaks towards lower 2θ with increasing Sn content is consistent with the replacement of Ti^{4+} (0.605 Å) by the larger Sn^{4+} (0.69 Å). Furthermore, the expanded XRD patterns (Figure 3a) reveal an apparent coexistence of multiple symmetries at room-temperature for $x \leq 0.14$, as corroborated by the broadening of peaks. Full pattern Rietveld refinement was performed for all compositions, as shown in Figure S3 (Supplemental Information), using orthorhombic (O, *Amm2*), tetragonal (T, *P4mm*), rhombohedral (R, *R3m*) and

cubic (C, $Pm\bar{3}m$) phases, the corresponding results are listed in Figure 3(b) and Table S1 (Supplemental Information). A mixture of O (68%) and T (32%) was refined for x = 0.05, yielding an excellent good of fitness (GOF) ~ 1.86. With the increase of Sn concentration, a higher amount of T (53%) phase (O phase ~ 47%) is found at x = 0.08. Coexistence of four phases (C, T, R and O) is observed in x = 0.11. The fraction of dominant C phase (86% for x=0.14) increases continuously and becomes the sole phase x = 0.18. The coexistence of crystal symmetries as determined from refinement of the X-ray data agrees with results gathered by a combination of other techniques. For example, the gradual decrease in T phase content with increasing x and its complete absence in x=0.14 is commensurate with the disappearance of the sharp mixed mode $E(LO_2 + TO_3) + B_1$ at 303 cm^{-1} from the Raman spectra as shown in Figure S4 (Supplemental information).[30] The presence of R is consistent with a residual $A_1(TO)$ mode at 185 cm^{-1}, but also it is expected from evolution of the permittivity behavior as depicted in Figure 3(c,d). The occurrence O symmetry is difficult to ascertain from the Raman data, however it is readily discerned from the high-resolution scanning transmission electron microscopy (HRSTEM) images, as shown later in Figure 5. The C phase expected far above the permittivity maximum, is an average structure, because the occurrence of modes in the Raman spectra is sufficient to rule out a truly centrosymmetric symmetry.
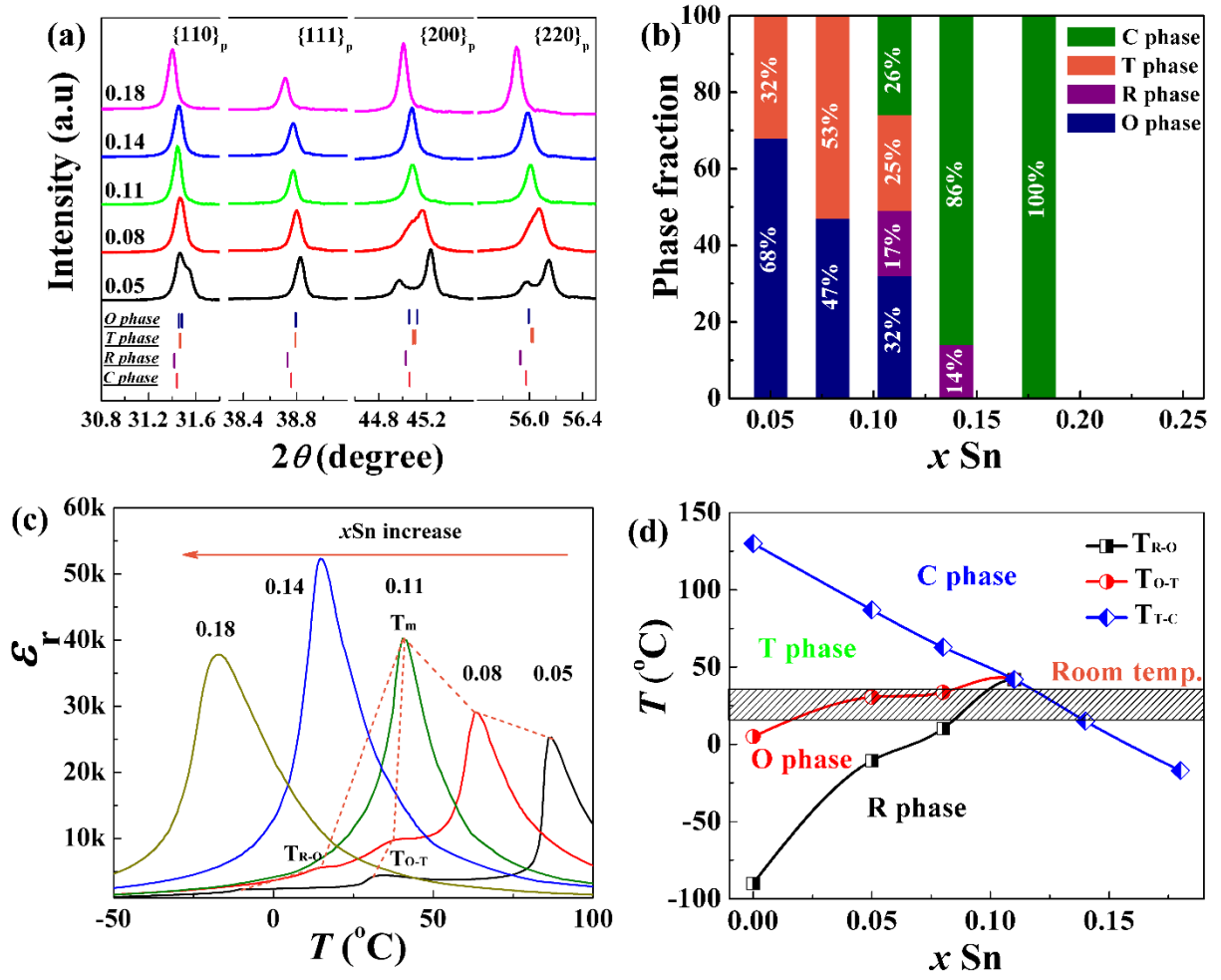
Figure 3 (a) Enlarged $\{110\}_p$, $\{111\}_p$, $\{200\}_p$ and $\{220\}_p$ peaks in the XRD patterns of BTSx. (b) phase fraction in BTSx as a function of x. (c) temperature dependence of dielectric permittivity (ε_r) for BTSx. (d) phase diagram of BTSx as function of x.

A continuous phase transition can also be clearly observed in the temperature dependence of dielectric permittivity (ε_r) and loss (tan δ), as shown in Figure 3c and Figure S5 (Supplemental Information). It is clear that with the increase of Sn content, T_m is found to decrease linearly from 87°C for $x = 0.05$ to -17°C for $x = 0.18$, with a gradual pinching of both phase transition temperatures of R to O phase (T_{R-O}) and O to T phase (T_{O-T}) close to room temperature (Figure 3a). Based on the results of XRD and temperature dependence of ε_r and tan δ, a phase diagram of BTSx as function of Sn concentration is schematically plotted, as shown in Figure 3(d), which clearly indicates that four phases, C, T, R and O, coexist near room temperature, in consistent with the DFT calculation (Figure 1b), Landau free-energy profile (Figure 2d,f) and XRD results (Figure 3a,b). The relaxor behavior of BTSx is analyzed

using the modified Curie-Weiss law and the corresponding results are plotted in Figure S6 (Supplemental Information). The degree of diffuseness (γ) is found to increase from 1.42 for $x = 0.05$ to 1.80 for $x = 0.18$, indicative of an enhanced relaxor behavior by Sn doping, in agreement with the Landau phenomenological theory and phase field simulation (Figure 2).

The d_{33} and planar eletromechanical coupling constant (k_p) of BTSx ceramics as function of x are shown in Figure 4(a). It is clear that values of d_{33} and k_p for BTSx ceramics are significantly enhanced by Sn doping, with the maximum values of $d_{33} \sim 1120$ pC/N and $k_p \sim 0.55$ achieved at $x = 0.11$. Furthermore, the maximum piezoelectric strain coefficient dS/dE, quasi-static positive and negative maximum d_{33} (d_{33}^{Emax} and $-d_{33}^{Emax}$) exhibit even larger values of 1700, 2180 and 1720 pm/V (Figure 4b,c), respectively, further confirming the ultrahigh piezoelectricity. On the other hand, the *ex-situ* temperature dependence of d_{33} and k_p for BTSx ($x = 0.11$) indicates that the piezoelectricity is stable until T_m is reached, above which it drops dramatically (Figure 4d), which is also further confirmed by the *in-situ* temperature dependence of dS/dE, d_{33}^{Emax} and $-d_{33}^{Emax}$ (Figure 4e,f). Room temperature d_{33} of BTS$_x$ ($x = 0.11$) is compared with that of other lead-free piezoelectrics and several typical PZT compositions and given in Figure 4(g,h). Our giant d_{33} value of $\sim$1120 pC/N is about twice that of other BT-based, KNN-based systems and soft PZTs encompassing only R+T or R+O+T mixed phases, such as 620 pC/N for BTZ-0.5BCT (Figure 4g),[20] 570 pC/N for $0.95K_{0.6}Na_{0.4}Nb_{0.965}Sb_{0.035}O_3$-$0.02BaZrO_3$-$0.03Bi_{0.5}K_{0.5}HfO_3$ (Figure 4h)[15] and 590 pC/N for ultrasoft PZT5H (Figure 4h),[31] which is currently the highest value reported in lead-free materials.
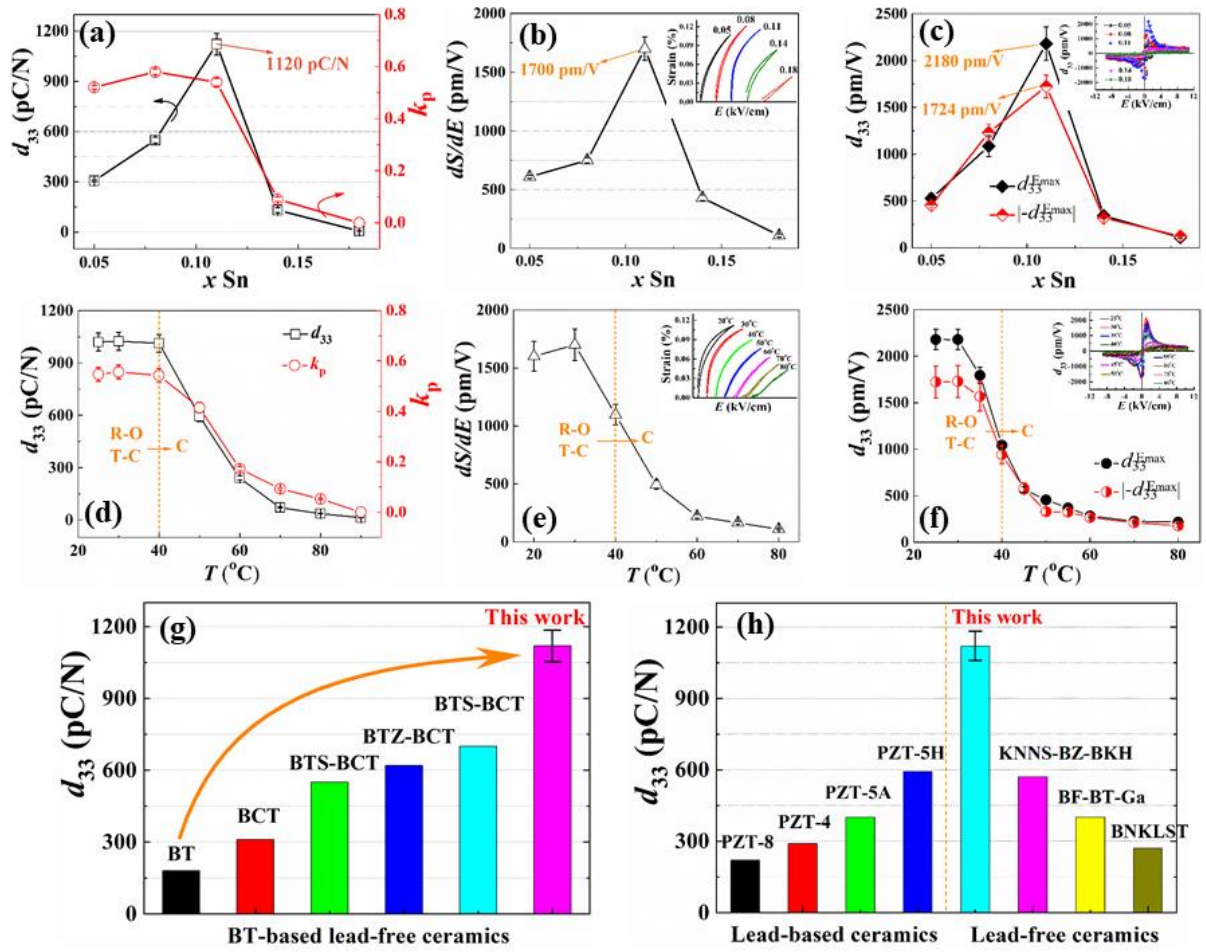
Figure 4 (a) The piezoelectric coefficient d_{33} and the planar eletromechanical coupling coefficient k_p. (b) the unipolar strain *vs.* electric field (*S-E*) loops and corresponding maximum converse piezoelectric coefficient dS/dE. (c) bias field d_{33}^* *vs.* electric field (d_{33}^*-E) hysteresis loops and corresponding quasi-static positive and negative maximum d_{33} (d_{33}^{Emax} and $-d_{33}^{Emax}$) of BTSx ceramics as function of x. The temperature dependence of (d) d_{33} and k_p, (e) *S-E* loops and dS/dE, (f) d_{33}^*-E loops, d_{33}^{Emax} and $-d_{33}^{Emax}$. The comparison in the room temperature d_{33} of BTSx ($x = 0.11$) with (g) BT-based piezoelectrics[20,31-35] and (h) several typical PZT and lead-free piezoelectrics.[14-17,21,36]

Figure 5 displays the microstructure of BTSx ($x = 0.11$). No micron-sized domains exist in the grain (Figure 5a), which is in consistence with the relaxor nature of BTSx ($x = 0.11$) (Figure S6, Supplemental Information). In order to examine whether the structural heterogeneity, if any, is attributed to the chemical inhomogeneity, the energy dispersive X-ray (EDX) mapping was carried out in a very small area shown in Figure 5(b). All four elements appear to be uniformly distributed, excluding any possible role played by the chemical segregation. Furthermore, the dipoles are mapped out based on the same HRSTEM micrograph, as shown in Figure 5(c). As explained earlier, R, T and O phases feature different polarization directions. The left portion in Figure 5(c) with dipoles pointing

11

to <110> could be an O domain, while the right portion having dipoles aligned along <100> direction is most likely to be T phase. It should be noted that the left nano-domain might also be R since the polar vectors in R and O are indiscernible under <001> zone axis. Nevertheless, a O phase is more likely because in this particular composition its phase fraction almost twice that of R phase (Figure 3b). The region between the two nano-domains should be regarded as a domain boundary, which is also an inter-phase interface.
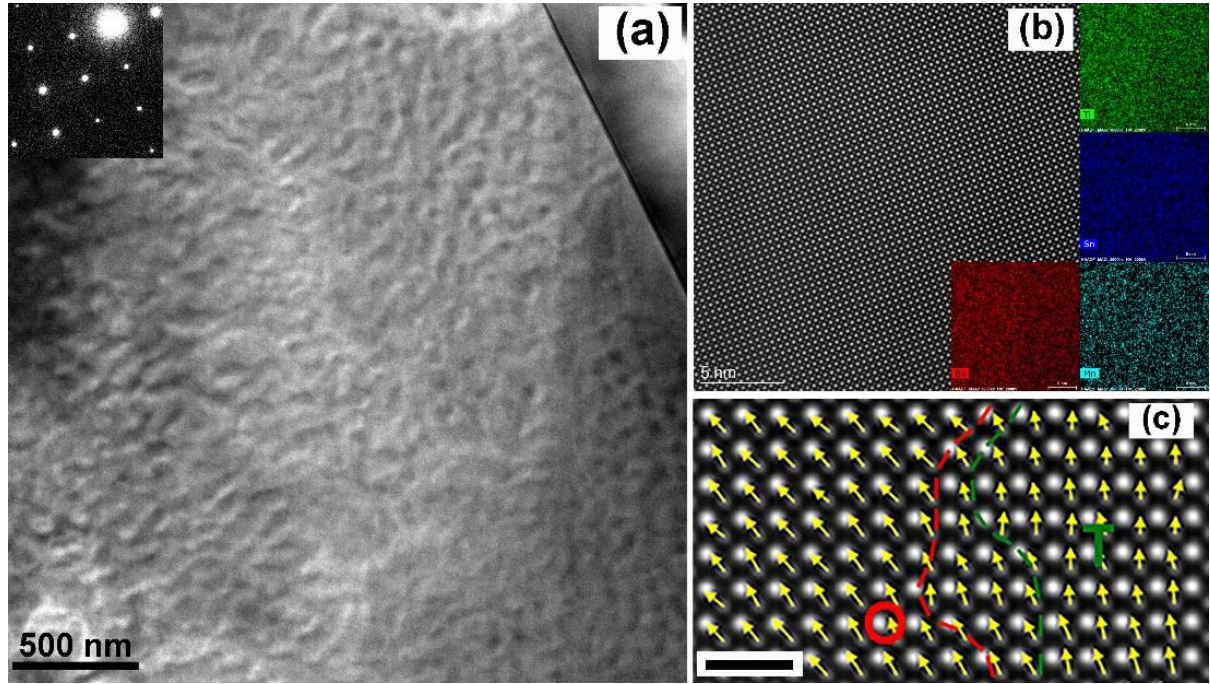
Figure 5 (a) Bright-field TEM micrograph of the domain structure in BTSx ($x = 0.11$) observed along <001> zone axis. (b) EDX mapping of Ba, Ti, Sn and Mn based on the HAADF-STEM image. (c) Ti cation displacement mapping within two neighboring domains. The scale bar measures 1 nm.

Conclusions

This work provides a new methodology and feasible solution to design materials with a record high piezoelectric coefficient among lead-free piezoelectrics. The first-principles calculations combined with Landau phenomenological theory and phase field simulation are powerful tools to design, calculate and simulate compositions, crystal structures, microstructures, energies etc. in ferroelectrics, with respect to different material systems and dopants. Indeed, a giant piezoelectric coefficient $d_{33} >$ 1100 pC/N is achieved in Sn-doped BaTiO$_3$ (BTS$_x$) ($x = 0.11$) ceramics, which is the highest value reported for lead-free ceramics. This remarkable enhancement of the piezoelectricity can be ascribed

to the strategic design of a flat Gibbs free energy density profile via a synergistic approach that involves both coexistence of multiple phases (CMP) and local structural heterogeneity (LSH). The occurrence of these two mechanisms is confirmed by crystal structure, microstructure and property characterization of BTS$_x$ ceramics. Hence this synergistic approach that combines macroscopically CMP with microscopically LSH may pave the way to halt the dominant role of lead-based ceramics in piezoelectric applications. Moreover, we would like to emphasize that the proposed strategy to enhance the piezoelectricity is not limited to ferroelectrics but could be further generalized to use for understanding and optimizing a wide range of functionalities.

Experimental

Sample preparation

Ba(Ti$_{1-x}$Sn$_x$)O$_3$+0.6% MnO$_2$ (x = 0.05, 0.08, 0.11, 0.14, and 0.18) ceramics were prepared by the conventional solid-state reaction method, where MnO$_2$ is used to reduce to conductivity. Dried high purity raw materials of TiO$_2$ (99.95%), SnO$_2$ (99.9%), BaCO$_3$ (99.9%) and MnO$_2$ (99%) were weighed stoichiometrically and ball-milled in an ethanol solvent using yttria-stabilized zirconia medium for 24 h. Subsequently, the dried mixture was ground and calcined at 1150 °C for 4 h, followed by further milling for 16 h. Powders were dried, mixed with 6 wt% polyvinyl alcohol (PVA) and then pressed into pellets of 12 mm in diameter and 1 mm in thickness under a uniaxial pressure of 80 MPa. Green pellets were sintered at 1380°C for 4 h in air after binder burn-out at 550 °C. Surfaces of as-sintered ceramics were ground and silver paste electrode was applied and fired at 600 °C for 10 min. The electric poling was carried out by applying a dc field of 4 kV/mm for 10 min in a silicone oil bath.

Characterization

The crystal structure of crushed and ground ceramic powder was analyzed by X-ray diffraction (XRD, Bruker D2 Phaser, Germany) with a Cu Kα radiation. An FEI Titan Themis 300 probe-corrected scanning transmission electron microscopy (STEM) operated at an accelerating voltage of 200 kV, equipped with a Super-X energy dispersive X-ray spectroscopy (EDX) detector, was employed for TEM observation and EDX acquisition. High-angle annular dark-field (HAADF) images were captured using a sub-angstrom electron probe with a convergence angle of 18 mrad and a detection angle of 99-200 mrad. The atomic positions of both A-site and B-

site columns were determined by fitting the intensity maxima in these images using a 2D Gaussian function. The off-center displacements of Ti cations were calculated with respect to the geometric center of the four surrounding A-site columns and overlaid on the HAADF images. The detailed description of the homemade code can be found elsewhere.[37] The piezoelectric coefficient (d_{33}) of poled pellets was measured by a Berlincourt meter (ZJ-3A, China). The planar electromechanical coupling coefficient k_p and dielectric properties was measured by a precision impedance analyzer (HP 4294A, Agilent, USA) under a temperature range of -50 to 150 °C. A ferroelectric tester system (TF Analyzer, 2000HS, aixACCT Systems GmbH, Aachen, Germany) was employed for the ferroelectric, piezoelectric and strain measurements, including electric-field induced unipolar/bipolar strain (S-E), polarization (P-E) hysteresis loops and bias field $d_{33}{}^*$(E) hysteresis loops (AC signal of 10 V at 250 Hz).

First-principles calculations

The first-principles calculations were carried out based on density functional theory (DFT), the pseudopotential method, and plane-wave basis sets.[38,39] The results reported in this paper were obtained with the use of the Cambridge serial total energy package (CASTEP).[40] The exchange-correlation effects were treated with the generalized gradient approximation (GGA).[41] For the modeling of the $BaTi_{1-x}Sn_xO_3$ ($0 \leq x \leq 0.2$) solid solutions, we have adopted the virtual crystal approximation (VCA), which implies preserving the same crystalline unit cells as $BaTiO_3$ and replacing the transition metal Ti with a virtual Sn atom.[42,43] A plane-wave cutoff energy of 800 eV was employed in the calculations, which assured a total energy convergence of 10^{-6} eV/atom. For the bulk calculations in which primitive unit cells were employed, the Brillouin zone sampling was set with the $8 \times 8 \times 8$ Monkhorst-Pack k-points meshes. All the primitive unit cells were allowed to fully relax until the force on each atom was smaller than 0.01 eV/Å.

Landau free energy modeling within our multiphase model from first-principles

To analyze the high electromechanical properties of the relaxor within our multiphase coexistence model, we employ Landau-Devonshire (LD) theory within the 6th-order terms of polarization. The free energy of a ferroelectric can be written in terms of the polarization components (P_x, P_y, P_z) as follows.[41-43]

$$
\begin{aligned}
F(\vec{P}) = {} & F_0 + \alpha(P_x^2 + P_y^2 + P_z^2) + \beta_1(P_x^4 + P_y^4 + P_z^4) \\
& + \beta_2(P_x^2 P_y^2 + P_y^2 P_z^2 + P_z^2 P_x^2) + \gamma_1(P_x^6 + P_y^6 + P_z^6) \\
& + \gamma_2[P_x^4(P_y^2 + P_z^2) + P_y^4(P_z^2 + P_x^2) + P_z^4(P_x^2 + P_y^2)] + \gamma_3 P_x^2 P_y^2 P_z^2,
\end{aligned}
\tag{1}
$$

where parameters α, β_1, β_2, γ_1, γ_2, and γ_3 are the coefficients of different orders of polarization $\boldsymbol{P}$. $F(\vec{P})$ represents the free energy at a certain temperature and composition as a function of polarization. F_0 denotes the free energy of a paraelectric phase. For our multiphase model for four-phase coexistence with the tetragonal (T), rhombohedral (R), orthorhombic (O), and cubic (C) phases, the free energy of each phase is the same, and the first deviation of the free energy for a certain phase is zero in order to make the phase stable. For simplicity, we assume that polarizations in three different ferroelectric phases have the same length but with different orientations, and we can then write

$$F(\vec{P_T}) = F(\vec{P_O}) = F(\vec{P_R}) = F(\vec{P_C}) = F_0, \tag{2}$$

and $dF(\vec{P})/d(\vec{P}) = 0$ (at $\vec{P} = \vec{P_T}, \vec{P} = \vec{P_R}, \vec{P} = \vec{P_O}$) \hfill (3)

where $\vec{P_T} = P_0 * (0,0,1)$, $\vec{P_R} = P_0 * (\frac{1}{\sqrt{3}}, \frac{1}{\sqrt{3}}, \frac{1}{\sqrt{3}})$, $\vec{P_O} = P_0 * (0, \frac{1}{\sqrt{2}}, \frac{1}{\sqrt{2}})$

Based on Eqs. (2) and (3), the free energy can be rewritten as

$$F(\vec{P}) = F_0 + \gamma_1 P_0^4 P^2 - 2\gamma_1 P_0^2 P^4 + \gamma_1 P^6, \tag{4}$$

Phase field simulations

In phase field simulations a ferroelectric system with local phase fluctuation,[44] the temporal evolution of a polarization field is described by the Time-Dependent Ginzburg-Landau (TDGL) equation,

$$\frac{\partial P_i(\mathbf{r}, t)}{\partial t} = -L \frac{\delta F}{\delta P_i(\mathbf{r}, t)}, \quad (i = 1,2,3), \tag{5}$$

where L is the kinetic coefficient, F, the total free energy of the system, $\mathbf{r}$, space position, and $P_i(\mathbf{r}, t)$ is the polarization. $\delta F / \delta P_i(\mathbf{r}, t)$ is the thermodynamic driving force for the spatial and temporal evolution of $\delta P_i(\mathbf{r}, t)$. The total free energy of the system includes the bulk free energy, elastic energy, electrostatic energy, and the gradient energy:

$$F = \int_V [f_{bulk} + f_{elas} + f_{elec} + f_{grad}] dV \tag{6}$$

where V is the system volume, f_{bulk} denotes the Landau bulk free energy density, f_{elas} the elastic energy density, f_{elec} the electrostatic energy density and f_{grad} the gradient energy density. The bulk free energy density is expressed by Landau theory as

$$
\begin{aligned}
f_{bulk} = {} & \alpha_1(P_1^2 + P_2^2 + P_3^2) + \alpha_{11}(P_1^4 + P_2^4 + P_3^4) + \alpha_{12}(P_1^2 P_2^2 + P_2^2 P_3^2 + P_3^2 P_1^2) \\
& + \alpha_{111}(P_1^6 + P_2^6 + P_3^6) + \alpha_{112}[P_1^4(P_2^2 + P_3^2) + P_2^4(P_1^2 + P_3^2) + P_3^4(P_1^2 + P_2^2)] \\
& + \alpha_{123} P_1^2 P_2^2 P_3^2
\end{aligned}
\tag{7}
$$

where α_1, α_{11}, α_{12}, α_{111}, α_{112} and α_{123} are Landau energy coefficients. The values of these coefficients determine the thermodynamic behaviors of the bulk phases. Based on experimental data (phase transition temperatures and dielectric properties), the Landau coefficients of BST ($x = 0\sim0.2$) are set to be:

$\alpha_1 = 2.34 \times 10^5 \ (T\text{-}381\text{+}700x) \ C^{-2}m^2N,$

$\alpha_{11} = 4.69 \times 10^6(T\text{-}393\text{+}700x)\text{-}2.18 \times 10^8 \ C^{-4}m^6N,$

$\alpha_{12} = 1.83 \times 10^8 \ C^{-4}m^6N,$

$\alpha_{111} = \text{-}6.52 \times 10^7(T\text{-}393\text{+}700x)\text{+}2.96 \times 10^9 \ C^{-6}m^{10}N,$

$\alpha_{112} = 1.77 \times 10^8 \ C^{-6}m^{10}N,$

$\alpha_{123} = 1.\,3 \times 10^8 \ C^{-6}m^{10}N.$

The parameters in the elastic, electrostatic and gradient energy density are assumed to be uniform throughout the system.[45] The gradient energy density, associated with the formation and evolution of domain walls, can be expressed as

$$f_{grad} = \frac{1}{2}G_{11}(P_{1,1}^2 + P_{2,2}^2 + P_{3,3}^2) + G_{12}(P_{1,1}P_{2,2} + P_{2,2}P_{3,3} + P_{1,1}P_{3,3})$$
$$+ \frac{1}{2}G_{44}[(P_{1,2} + P_{2,1})^2 + (P_{2,3} + P_{3,2})^2 + (P_{1,3} + P_{3,1})^2] \tag{8}$$
$$+ \frac{1}{2}G_{44}'[(P_{1,2} - P_{2,1})^2 + (P_{2,3} - P_{3,2})^2 + (P_{1,3} - P_{3,1})^2]$$

where G_{ij} are gradient energy coefficients. $P_{i,j}$ denote $\partial P_i/\partial r_j$. The gradient energy coefficients are chosen to be $G_{11} / G_{110}=1.2$, $G_{12} / G_{110}=0$, $G_{44} / G_{110}= G_{44}' / G_{110}=0.6$, where $G_{110}=7.04\times10^{-11}C^{-2} \ m^4N$. The time step for integration is $\Delta t / t_0 = 0.01$, where $t_0 = 1/L\alpha_1\big|_{T=300\ K}$. The corresponding elastic energy density can be expressed as:

$$f_{elas} = \frac{1}{2}c_{ijkl}e_{ij}e_{kl} = \frac{1}{2}c_{ijkl}(\varepsilon_{ij} - \varepsilon_{ij}^0)(\varepsilon_{kl} - \varepsilon_{kl}^0) \tag{9}$$

where c_{ijkl} is the elastic stiffness tensor, ε_{ij} the total strain, ε_{kl}^0 the electrostrictive stress-free strain, i.e., $\varepsilon_{kl}^0 = Q_{ijkl}P_kP_l$. The elastic constants and electrostrictive coefficients of $BaTiO_3$ are used in the simulations A semi-implicit Fourier-spectral method is adopted for numerically solving the TDGL equation. In the computer simulations, 2D 64×64 discrete grid points and 3D 64×64×64 discrete grid points are employed. The grid space in real space is chosen to be $\Delta x = \Delta y = \Delta z = 1$ nm. Periodic boundary conditions are used to simplify numerical calculations.

Acknowledgements

Competing interests

The authors declare no competing interests.

References

1.   Zhang, S*., et al.*, *Progress in materials science* (2015) **68**, 1
2.   Jaffe, B., *Piezoelectric ceramics*. Elsevier: 2012
3.   Haertling, G. H., *J Am Ceram Soc* (1999) **82** (4), 797
4.   Label, P. I*., et al.*, (2005)
5.   Shrout, T. R., and Zhang, S. J., *Journal of Electroceramics* (2007) **19** (1), 113
6.   Rödel, J*., et al.*, *J Am Ceram Soc* (2009) **92** (6), 1153
7.   Wang, D*., et al.*, *Journal of advanced dielectrics* (2018), 1830004
8.   Wang, D. W*., et al.*, *J Eur Ceram Soc* (2017) **37** (4), 1857
9.   Wang, D. W*., et al.*, *ACS Appl Energ Mater* (2018) **1** (8), 4403
10.   Wang, D. W*., et al.*, *J Mater Chem A* (2018) **6** (9), 4133
11.   Murakami, S*., et al.*, *J Eur Ceram Soc* (2018) **38** (12), 4220
12.   Murakami, S*., et al.*, *J Am Ceram Soc* (2018) **101** (12), 5428
13.   Chandarak, S*., et al.*, *Journal of Superconductivity and Novel Magnetism* (2012) **26** (2), 455
14.   Saito, Y*., et al.*, *Nature* (2004) **432** (7013), 84
15.   Xu, K*., et al.*, *Advanced Materials* (2016) **28** (38), 8519
16.   Wang, D. W*., et al.*, *J Am Ceram Soc* (2017) **100** (2), 627
17.   Liu, Q*., et al.*, *Energ Environ Sci* (2018) **11** (12), 3531
18.   Zheng, T*., et al.*, *Energy Environ Sci* (2017) **10** (2), 528
19.   Xu, K*., et al.*, *Adv Mater* (2016) **28** (38), 8519
20.   Liu, W. F., and Ren, X. B., *Phys Rev Lett* (2009) **103** (25)
21.   Lee, M. H*., et al.*, *Advanced Materials* (2015) **27** (43), 6976
22.   Li, F*., et al.*, *Science* (2019) **364** (6437), 264
23.   Li, F*., et al.*, *Nat Mater* (2018) **17** (4), 349
24.   Haun, M. J*., et al.*, *Ferroelectrics* (1989) **99**, 13
25.   Fu, H. X., and Cohen, R. E., *Nature* (2000) **403** (6767), 281
26.   Damjanovic, D., *Ieee T Ultrason Ferr* (2009) **56** (8), 1574
27.   Neirman, S. M., *J Mater Sci* (1988) **23** (11), 3973
28.   Li, F*., et al.*, *Adv Funct Mater* (2018) **28** (37), 1801504
29.   Cross, L. E., *Ferroelectrics* (1987) **76** (1), 241
30.   Deluca, M*., et al.*, *J Mater Chem A* (2018) **6** (13), 5443
31.   Zhao, C. L*., et al.*, *J Am Chem Soc* (2018) **140** (45), 15252
32.   Wang, Z. M*., et al.*, *J Mater Sci-Mater El* (2016) **27** (5), 5047
33.   Sun, H. J*., et al.*, *J Alloy Compd* (2016) **670**, 262
34.   Yuan, R. H*., et al.*, *Advanced Materials* (2018) **30** (7)
35.   Acosta, M*., et al.*, *Appl Phys Rev* (2017) **4** (4)
36.   Berlincourt, D., Piezoelectric crystals and ceramics. In *Ultrasonic transducer materials*, Springer(1971), pp 63
37.   Ma, T*., et al.*, *arXiv preprint arXiv:1909.02536* (2019)
38.   Kohn, W., and Sham, L. J., *Physical review* (1965) **140** (4A), A1133
39.   Hohenberg, P., and Kohn, W., *Physical review* (1964) **136** (3B), B864
40.   Segall, M*., et al.*, *Journal of Physics: Condensed Matter* (2002) **14** (11), 2717
41.   Perdew, J. P*., et al.*, *Phys Rev Lett* (1996) **77** (18), 3865
42.   Liu, S.-Y*., et al.*, *Physical Chemistry Chemical Physics* (2017) **19** (33), 22190
43.   Liu, S. Y*., et al.*, *J Am Ceram Soc* (2016) **99** (10), 3336
44.   Chen, L. Q., *J Am Ceram Soc* (2008) **91** (6), 1835
45.   Li, F*., et al.*, *Nature communications* (2016) **7**, 13807